JGR Space Physics

RESEARCH ARTICLE
10.1029/2019JA027245

Magnetic Field Effect on Antenna Signals Induced by Dust Particle Impacts

L. Nouzák[1], Z. Sternovsky[2,3], M. Horányi[2,4], S. Hsu[2], J. Pavlů[1], M.-H. Shen[2,3], and S.-Y. Ye[5,6]

[1]Department of Surface and Plasma Science, Charles University, Prague, Czech Republic, [2]Laboratory for Atmospheric and Space Physics, University of Colorado, Boulder, CO, USA, [3]Department of Smead Aerospace Engineering Sciences, University of Colorado, Boulder, CO, USA, [4]Department of Physics, University of Colorado, Boulder, CO, USA, [5]Department of Physics and Astronomy, University of Iowa, Iowa City, IA, USA, [6]Department of Earth and Space Sciences, Southern University of Science and Technology, Shenzhen, Guangdong, China

Key Points:
- Dust impact signals can be significantly reduced for spacecraft floating potentials close to zero
- The magnetic field affects only the electron part of impact signals according to the magnetic field strength, its orientation
- For case of RPWS in D ring, experiment shows the low SC potential has a stronger effect on impact signals than the magnetic field of Saturn

Correspondence to:
L. Nouzák,
nouzak@aurora.troja.mff.cuni.cz

Citation:
Nouzák, L., Sternovsky, Z., Horányi, M., Hsu, S., Pavlů, J., Shen, M.-H., & Ye, S.-Y. (2020). Magnetic field effect on antenna signals induced by dust particle impacts. *Journal of Geophysical Research: Space Physics*, *125*, e2019JA027245. https://doi.org/10.1029/2019JA027245

Received 6 AUG 2019
Accepted 5 NOV 2019
Accepted article online 21 NOV 2019

Abstract The Radio and Plasma Wave Science instrument on Cassini has observed fewer than expected dust particle impacts during the mission's Grand Finale orbits. The relatively strong magnetic field in the close vicinity of the planet has been suggested to affect the intensity of the dust impact generated signals. A laboratory investigation is performed using dust particles accelerated to ≥20 km/s speed impacting onto a previously developed model of the spacecraft and the Radio and Plasma Wave Science antennas. The external magnetic field is generated by two sets of magnetic coils. The recorded antenna waveforms are decomposed into contributions from the electrons and ions of the dust impact generated plasma cloud. A good qualitative understanding of the waveforms is achieved by dividing the electron and ion population into two portions: one that is escaping from the spacecraft and another that is collected by the spacecraft. The experimental results show that the part of the signal corresponding to escaping electrons is affected by the magnetic field and that dust impact signals can be significantly reduced for spacecraft floating potentials close to zero.

1. Introduction

The Cassini spacecraft crossed Saturn's ring plane at various radial distances and provided valuable information of distribution and origin of the dust particles. Besides the dedicated Cosmic Dust Analyzer, the Radio and Plasma Waves Science (RPWS) instrument also performed in situ dust detection (Dong et al., 2015; Gurnett et al., 2004; Hill et al., 2012; Kempf et al., 2008, 2010; Kurth et al., 2006; Spahn et al., 2006; Srama et al., 2006; Wang et al., 2006; Ye et al., 2014; Ye, Gurnett, et al., 2016; Ye, Kurth, et al., 2016). The RPWS antennas detect the transient plasma clouds generated by the impact ionization of the dust particle and the surface material of the spacecraft (SC) body or the antennas. The frequency and amplitudes of detected signals allow estimating the dust density and size distribution. A recent study by Ye, Kurth, et al. (2016) found that the interpretation of the signals needs to consider the configuration of antennas (dipole vs. monopole).

On 26 April 2017, Cassini passed through the gap between the Saturn's main ring and its atmosphere/ionosphere starting the first (orbit #271) of the Grand Finale orbits. Due to concerns about the safety of the SC and onboard instruments, Cassini's high-gain antenna (HGA) was pointed into the ram direction in the first orbit in order to provide protection for the SC and its instruments from possible damages from high-speed dust particles impacts. The RPWS was designated to make dust measurement in this configuration and found a low density of micron-sized particles that was later confirmed also by Cosmic Dust Analyzer (Hsu et al., 2018; Ye et al., 2018). The in situ data set is important for the understanding of the dynamics of micron-sized grains between the D ring and Saturn's cloud tops.

The early RPWS observations considered that the relatively strong magnetic field in the close vicinity of Saturn may have reduced the amplitudes of the dust impact signals by preventing electrons from the impact plasma to escape from the SC (Ye et al., 2018). This suggestion was the motivation for the work described in this article. Following Dougherty et al. (2018), the magnetic flux density was about 18 μT in the ring plane crossing. This value corresponds to an electron gyroradius of approximately $r_g = 0.2$ m, which is smaller than the diameter of the HGA. The magnetic field thus may significantly reduce the ratio of electrons from the

impact plasma cloud that can escape from SC, reducing thus the amplitude of the corresponding antenna signals.

Antenna instruments have been used for the detection of dust particles since the Voyager era (Aubier et al., 1983; Gurnett et al., 1983), and there have been several models aiming at the understanding of the physical mechanism how measurable signals are generated (e.g., Meyer-Vernet et al., 2014, 2017; Oberc, 1996; Zaslavsky, 2015). Here we provide the summary of recent findings based on laboratory measurements that are precursors to the work presented in this article. Collette et al. (2015) carried out the first laboratory simulation measurements using a dust accelerator. This work has identified three signal-generating mechanisms: charge collection by the SC body, charge collection by the antenna from nearby dust impacts, and induced charging from the space charge of the expanding impact plasma cloud. Nouzák et al. (2018) expanded on the initial study by using a scaled-down model of the Cassini spacecraft with a combination of monopole and dipole antennas. The measurements demonstrated that the amplitudes and polarities of the impact signals depend on the bias voltage applied onto the antennas or the SC body and confirmed the dominant mechanisms of signal generation from Collette et al. (2015). A supporting measurement was carried out by Collette et al. (2016) investigating the effective temperatures of electron and ion components of the impact plasma. This study found that the temperature of the electrons is about 1 eV and independent of the dust impact speed. On the other hand, the temperature of ions increases from 5 eV at 4 km/s impact speed to ≈20 eV at 20 km/s. The temperatures of these two components play a determining role in how the antenna signals are affected by the floating potential of the SC body, where the impacts occur.

The fundamental quantity driving the generation of impact-induced antenna signals is the impact charge—the charge in a small plasma cloud that is generated by the high-velocity impact of the dust particle. The charge yield has been characterized in the laboratory over wide ranges of mass and velocity using dust accelerator facilities (e.g., Auer, 2001; Auer & Sitte, 1968; Burchell et al., 1999; Dietzel et al., 1973; Friichtenicht, 1962; Iglseder & Igenbergs, 1987). The amount of impact charge generated depends on the speed (v_d) and mass (m_d) of the particle and the materials of the dust and target materials. It is usually described in a form of a power law, $Q_{imp} \cong \alpha m_d v_d^{\beta}$, where parameters α and β are determined through laboratory calibration measurements. Collette et al. (2014) provided a recent summary of impact charge yields, including common SC materials. For historical reasons, the dust target material combination used in the experiments described below is Fe-W. For this combination the charge yield has been measured by Dietzel et al. (1972) over a velocity range of 2–40 km/s and found to be of a form

$$Q_{imp}[\mathrm{C}] \cong 0.51 m_d[\mathrm{kg}] v_d^{3.5} \left[\frac{\mathrm{km}}{\mathrm{s}}\right]. \quad (1)$$

Parameters Q_{imp}, m_d, and v_d are measured in units as indicated.

2. Experimental Setup

The measurements were carried out using the electrostatic dust accelerator at the University of Colorado (Shu et al., 2012). Briefly, an electrostatic field generated by $U_{acc} = 2.2$ MV potential is used to accelerate micron- and submicron-sized charged dust particles to velocities of 1–100 km/s. In the beamline, each accelerated particle is detected and characterized using a set of pickup tube detectors connected to sensitive electronics (Srama & Auer, 2008). The amplitude and the duration of the induced charge signals provide the charge and the speed on the dust particle. The mass and size are then calculated using the acceleration voltage from energy conservation. An field programmable gate array-based cross-correlation filter is employed for down-selecting particles based on preprogrammed mass and velocity ranges before allowing them into the experimental chamber (Thomas et al., 2013).

The main experimental chamber (1.2 m in diameter and 1.5 m long) has been equipped with two set of coils generating nearly homogenous magnetic field in the center (Figure 1). A field perpendicular to the trajectory of dust particles ($B_{\perp}$) is generated by a pair of coils in a Helmholtz configuration that is wound directly onto the cylindrical chamber. The 16 turns of copper wire in each coil with 40 A of current generates $B_{\perp} = 1.45$ mT field in the center of the chamber, as measured using a Hall effect sensor. A second set of coils is used for generating a magnetic field parallel to the dust beam ($B_{\parallel}$). These coils are 1.2 m in diameter, separated by

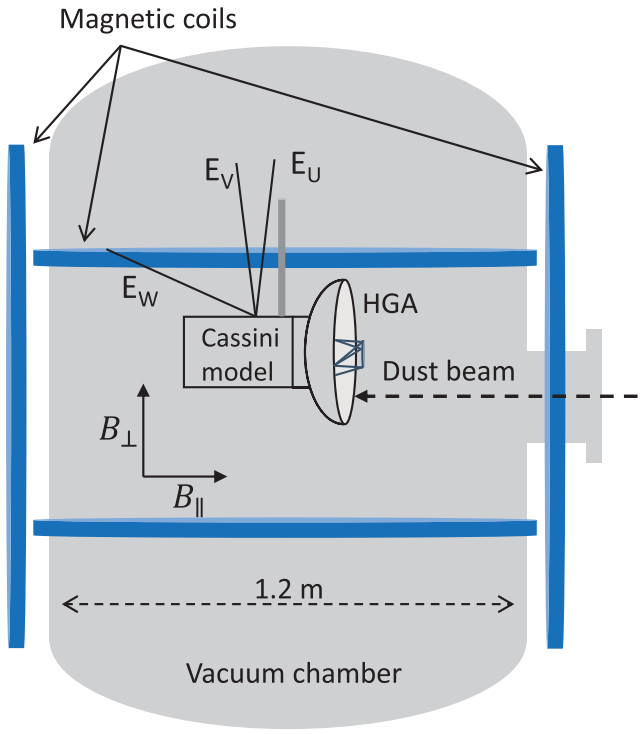

Figure 1. The experimental setup with the reduced-size model of the Cassini spacecraft installed in the experimental chamber. Two magnetic coils are used to generate fields: Parallel ($B_{||}$) and perpendicular ($B_{\perp}$) to the dust beam. The figure is not to scale. See text for details.

1.2 m, and are attached to the two sides of the chamber using mechanical fixtures. There are 32 turns in each coil generating $B_{\perp} = 1.45$ mT field with 60 A of current. At these currents and field intensities, the coils can be operated continuously and without cooling. By the combination of the two sets of coils, a magnetic field of any orientation (within the horizontal plane) can be generated, although this capability has not been exercised in the present experiments, and only purely parallel or purely perpendicular fields have been applied.

The impact experiments are performed using the 1:20 scaled-down model of the Cassini spacecraft used in previous studies and described in detail by Nouzák et al. (2018). The model consists of the HGA (17.5 cm in diameter), a cylindrical SC body (20 cm in length), and the magnetometer boom. The three model antennas (E_U, E_V, and E_W) are mounted similarly as those of RPWS instrument on Cassini (Gurnett et al., 2004). In the model setup the E_U and E_V antennas are configured as a dipole, and E_W is operated as a monopole. The sensing electronics are instrumentation amplifiers that measure the potential differences $U_U - U_V$ and $U_W - U_{SC}$ of the transient dust impact signal. Here SC denotes the spacecraft body that includes the HGA. The amplifiers are housed inside the cylindrical SC body, have bandwidths of 50 Hz–100 kHz, and gains of 100 (Nouzák et al., 2018). The time-response of the amplifier is sufficiently fast to resolve the antenna signals from impacts onto the HGA. The antennas and the SC are connected to the amplifier inputs using ac-coupling capacitors, which allow applying bias potentials to the sensing elements to imitate the floating potential of the SC and antennas attained in space.

The HGA is pointed into the dust beam, as shown in Figure 1. The dust impacts occur on a 2.5×2.5 cm^2 tungsten foil attached to the HGA, close to the edge. Tungsten is selected for high impact charge yield and direct comparability with previous measurements (e.g., Nouzák et al., 2018). The dust beam is pointed at the middle of the tungsten foil, at 15 mm from the edge of the HGA. The dust impacts are spatially spread over a 10 mm diameter circular area. Due to the curvature of the HGA, the impacts occur at about a 27° angle, measured from surface normal.

The magnetic field intensity is set to 0, 0.35, or 1.45 mT and is oriented either parallel or perpendicular to the dust beam, as shown in Figure 1. The latter two values correspond to electron Larmor radii of $r_L = 9.6$ and 2.3 mm, respectively, assuming 1 eV electron energy. (The effect of Earth's magnetic field is neglected.) The setup is thus designed to investigate conditions, where the electron Larmor radius is small and/or much smaller in comparison with the characteristic size of the HGA antenna (200 mm diameter) and the distance of the impact location to the edge of the HGA. In comparison, the ion Larmor radius is much larger, on the order of 1 m, and thus the trajectories of ions are only weakly influenced by the magnetic field. Four different bias voltages are applied uniformly to the SC and the antennas: 0, ±5, and −20 V. The negative bias voltages intend to simulate conditions, where charging from the ambient plasma dominates over photoelectron emission. The +5 V bias potential simulates conditions during the closest approach of the Grand Finale orbits, as characterized by the Langmuir probe onboard (Jacobsen et al., 2009). The reference is the 0 V bias case, where the impact plasma is expanding freely, influenced only by the magnetic field, if present.

The performed dust impact experiments are limited to a velocity range of 20–40 km/s that is similar to the values encountered during the Grand Finale orbits at the closest approach to Saturn. Based on the findings by Collette et al. (2016), the ion and electron temperatures are expected to around 20 and 1 eV, respectively.

The signals from the amplifier are recorded using a fast digitizing oscilloscope and are numerically filtered. The results confirmed the finding by Nouzák et al. (2018) that in case of dust impacts on the SC body (including the HGA), the dominant signal is measured between the monopole antenna E_W and the SC, that is, $\Delta U_{W-SC} = U_W - U_{SC}$. Only this signal is analyzed further. The charge responsible for generating the recorded voltage is calculated as $Q = UC_{SC}/g$, where $g = 100$ is the gain of the amplifier and $C_{SC} = 120$ pF

is the capacitance of the model SC body (Nouzák et al., 2018). The parameters of the accelerated dust particles, including the mass, the velocity, and the charge carried by the particle (Q_d), are provided by the accelerator facility for each impact event.

3. Experimental Results and Analysis

3.1. Waveform Overview

Figure 2 is an overview of the characteristic waveforms for different applied bias voltages (0, ±5, and −20 V), and without an external magnetic field ($B = 0$), as a baseline for the data interpretation and analysis to follow. The signal shapes are qualitatively similar to those reported by Nouzák et al. (2018), where impacts onto the antennas were investigated primarily. Briefly, there are two characteristic features in the waveforms: the fast *pre-spike signal*, followed by the longer *charge collection signal*. The pre-spike is generated by the fast-escaping electrons that leave behind a cloud with a positive net charge. This cloud of ions is registered as a positive potential on the SC and measured as a negative-going spike by the monopole antenna, $\Delta U_{W-SC} = U_W - U_{SC}$. The amplitude of the pre-spike is influenced by the applied bias potential as this determines the fraction of electrons that are energetic enough to overcome the attractive force, when positive potential is applied onto the SC. The duration of the pre-spike is determined by the expansion speed of the ions, over which the positive space charge disappears from the vicinity of the SC body (Nouzák et al., 2018).

In each panel on Figure 2, the dashed black part of the signal follows an exponential decay. The amplitude of this signal is due to net impact charge that is collected on the SC body (denote hereafter as Q_{col}) and thus has to be discharged through the biasing resistor with an effective value $R = 5$ MΩ. The corresponding characteristic discharge time is thus $RC_{SC} = 5\ \text{M}\Omega \times 120\ \text{pF} = 0.6$ ms, which is in good agreement with the observations. In space, the discharge time is set by the parameters of the ambient plasma and the SC, as discussed by Zaslavsky (2015), O'Shea et al. (2017), or Ye et al. (2019), and the references therein.

3.2. Simple Signal Generation Model

Here we present a simple model describing the signals shown in Figure 2. First, it is assumed that the impact charge is composed in equal parts of electrons and ions, $Q_{imp} = Q_i = |Q_e|$ (Auer, 2001), where the negative charge of electrons is represented by $Q_e < 0$. (It is noted for completeness that a small fraction of the negative charge may be in the form of negative ions that are much heavier than electrons. Negative ions are neglected here, however.) Second, it is assumed that the electrons and ions of impact generated plasma decouple from one another shortly after the impact while still in the close vicinity of the SC body (O'Shea et al., 2017). Then both the electron and ion parts of the impact charge can be divided into two parts: the one that is collected on the SC and another that is escaping to the ambient environment:

$$\begin{aligned} Q_i &= Q_{i,esc} + Q_{i,col} \\ Q_e &= Q_{e,esc} + Q_{e,col} \end{aligned} \tag{2}$$

The ratio of escaping to collected particles is controlled by the energy distribution of the particles (both electrons and ions) and the potential of the SC.

The third assumption is that the escape or the collection of electrons occurs over a short time scale, that is, before the ions can move substantially. This assumption can be justified by much higher thermal speed of electrons due to the small mass. Under these three assumptions, the fast positive "charging" of the SC occurs due to the escaping electrons, when the SC is at zero, negative, or slightly positive potential, where the escape of electrons is energetically possible. A transient positive potential (known as pre-spike) thus establishes on the SC ($U = Q_{net}/C_{SC}$) that corresponding to the net charge of

$$Q_{net} = Q_i + Q_{e,col} = Q_i + \left(Q_e - Q_{e,esc}\right) = -Q_{e,esc}. \tag{3}$$

The positive charge of the ions residing in the vicinity of the SC is lessened by the fraction of electrons already collected on the SC. It is clear from the conservation of charge employed in equation (3) that the developed potential can also be described as due to the charge of escaping electrons, $Q_{e,esc}$. Figure 2 indicates the part of the waveforms that is due to escaping electrons. Please note that the signal measured is $U_W - U_{SC}$, and thus the potential of SC in Figure 2 appears inverted.

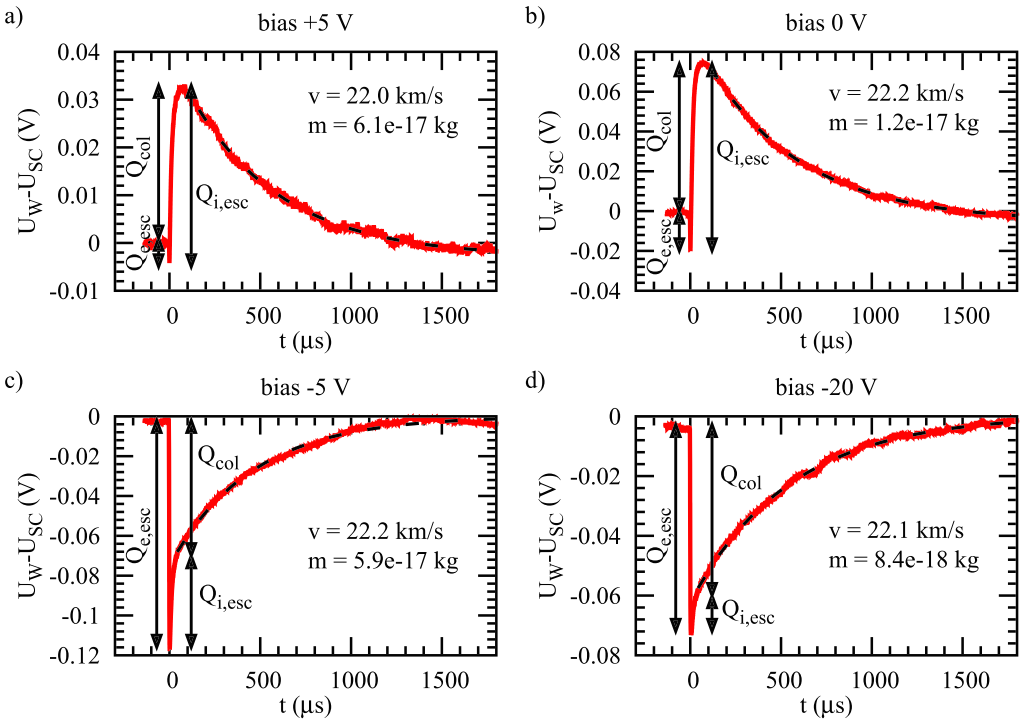

Figure 2. A set of characteristic impact signals ($U_W - U_{SC}$) measured at a +5, b 0, c −5 V, and d −20 V bias potentials applied to the spacecraft and antennas. Data are collected with no magnetic field applied ($B = 0$). The masses and velocities for each impacting particle are noted in the panel. The black dashed curve is an exponential decay with a time constant of $RC_{SC} = 0.6$ ms. The notation illustrates the interpretation of the different parts of the waveforms based on the simple model described in the text.

The next step in the signal generation process is to account for the motion of the ions, which takes place over a characteristic time scale of $\tau_i \approx L_{SC}/v_i$. Here v_i is the average speed of ions in the impact plasma, and L_{SC} is the characteristic size of the SC. Escaping ions result in the negative charging of the SC and is indicated in Figure 2. The physical explanation of the pre-spike signal is thus the fast escape of the electrons, followed by the escape of the ions. The duration of the pre-spike signal is on the order of τ_i, as already demonstrated by Nouzák et al. (2018). In summary, the pre-spike signal is generated by induced charge on the SC and does not affect the collected charge signal as long as the characteristic discharge time is much longer compared to τ_i. This may not be the case in dense plasmas, where discharge times are significantly lessened (Vaverka et al., 2019; Ye et al., 2018; Zaslavsky, 2015).

Once the escape and/or collection of ions is over, the resulting SC voltage is determined by the net collected charge:

$$Q_{col} = Q_{i,col} + Q_{e,col} = (Q_i - Q_{i,esc}) + (Q_e - Q_{e,esc}) = -(Q_{i,esc} + Q_{e,esc}) \quad (4)$$

As it is seen from this equation, the net collected charge also equals the negative value of the net escaping charge, as one would expect.

With the simple model presented above, the shapes of the signals in Figure 2 can be understood both qualitatively and quantitatively. For the case of +5 V bias voltage (Figure 2a), only a small fraction of electrons are energetic enough to escape from the SC. The large fraction of escaping ions then drives the SC to negative potential. In the laboratory measurements, the net collected charge is discharging through the electronic circuit. The zero-bias case (Figure 2b) is similar with both electron and ion escapes observed. For −5 V bias potential (Figure 2c) the fraction of escaping electrons is larger than that of ions, resulting in a net positive collected charge. Note that the pre-spike is still clearly visible, and its amplitude is proportional to $|Q_{i,esc}+Q_{e,esc}|$, that is the difference of the escaping electron and

ion fractions. The pre-spike is diminishing for the −20 V case (Figure 2d). This is because most of the ions are attracted back to the SC, and only a small fraction of them can escape.

It is also worth noting that while the four waveforms shown in Figure 2 are typical to the different bias potentials, there is a large variation between individual impacts even when they are of similar speed and mass. This applies for the generated impact charge and also the ratio of the escaping/collected fractions. The latter indicates that significant variations may exist also in the characteristic temperatures of the electron and ion components.

3.3. Effects of the Applied Bias Potential ($B = 0$)

Figure 3 shows the effect of the bias potential and magnetic field on the escaping electrons and ions following the data interpretation described above and shown in Figure 2. The escaping electron and ion charges are normalized to the mass for each event, following equation (1). Each point in the figures represents the median value from approximately 30 individual impact events at a given setting. The error bars are representing the first and third quartiles of each data set. The impact velocity is limited to a narrow range of 20–25 km/s. With this limitation the effect of velocity can be neglected since the velocity distribution is similar in each set.

3.3.1. Electron and Ion Impact Charges

Let us first discuss the normalized amplitudes of the escaping electron and ion fractions for zero magnetic field ($B = 0$). The largest amplitudes (about 1×10^4 C/kg) of escaping electron signals are observed for the −5 and −20 V bias cases (Figures 3c and 3d). These measured escaping electron charges can be considered to be close to the total impact charge, $Q_{imp} \cong |Q_{e,\ esc}|$. It is also of the same order as the $\approx 2 \times 10^4$ C/kg impact charge predicted from equation (1) at relevant velocities. The fraction of electrons escaping from the SC, however, varies strongly with more positive potentials. An interesting case is the 0 V bias, where the impact plasma expands freely. Figure 3a shows that on average about 35% of the electrons escape from the SC (compared to the cases with applied negative bias). This result can be interpreted as the electrons in the impact plasma are isotropic and about half of them will leave the SC after the expansion of the plasma is complete (e.g., Meyer-Vernet et al., 2017). Since dust impacts occurred within the HGA (Figure 1), the field of view for the escaping electrons is limited to less than 2π sr, which could explain why <50% of the electrons are escaping.

The largest escaping ion charge signals are observed at 0 and +5 V biases, where the ions are not retained by the attractive potential of the SC. The value of $Q_{i,esc}$ is about 0.5×10^4 C/kg (Figures 3e and 3f), that is about half of $|Q_{e,esc}|$. This is consistent with earlier observations reported by Auer (2001) that the positive part of the impact charge being up to a factor of three times lower than the negative part (Auer, 2001). There are several possible explanations, including the strong increase of Q_e with impact angle (Dietzel et al., 1972) or significant differences in the angular and/or velocity distributions of the two species.

3.3.2. Collected Charge

Since the electronics of antenna instruments deployed in space have limited bandwidths, in many cases the fast feature of the induced charge signal is not resolved. Leaving thus only the collected charge followed by the relatively slow discharge time observable in the waveforms (Figure 2). According to equation (4), the collected charge Q_{col} is the sum of the escaping electron and ion charges, which are both affected by the potential of the SC. As discussed above, for large SC potentials the collected charge will approach the electron or ion impact charges, depending on the polarity of the bias. At low SC potentials, however, the amplitude of the signal is significantly reduced. The collected charges are the lowest on average at or near 0 V bias, where $Q_{col} \ll Q_{imp}$ (Figures 3a and 3e), but the reduction is significant also for ±5 V biases. The consequence is that antenna instruments will report a deflated dust mass and/or mass and density distributions, when operating in environments where the SC floating potential is small.

3.3.3. Electron and Ion Temperatures

The data reported in Figure 3 are in agreement with previous measurements of the effective temperatures of electrons and ions from the impact plasma generated by Fe particles impacting on a W target. For example, the fraction of escaping electrons is reduced by >90% once a bias potential of +5 V is applied to the SC (Figures 3b and 3c). This result agrees with the findings by Collette et al. (2016) that the electron temperature in the impact plasma is on the order of 1 eV. For ions, the bias voltage increased to −5 and −20 V reduces the fraction of escaping ions to about 55% and 25%, respectively, compared to the 0 V bias case (Figures 3g and 3h). With the assumption that the energy distribution of ions follows a Boltzmann distribution, the

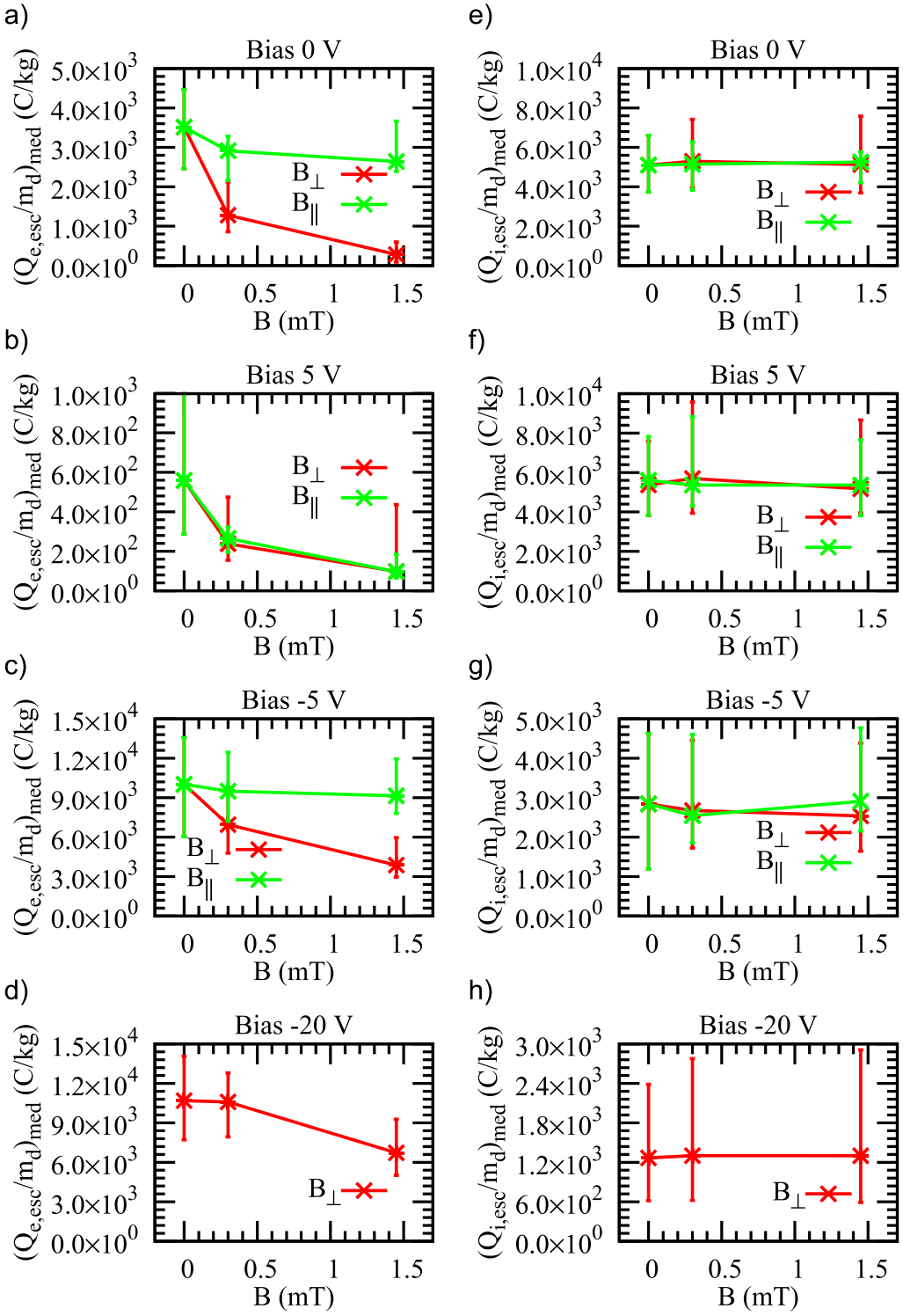

Figure 3. The effect of magnetic field on the electrons (panels a–d) and ions (panels e–h) escaping from the impact plasma. The results are shown for two magnetic field orientations ($B_\perp$ and $B_\parallel$) and different bias potentials (0, +5, −5, and −20 V). Absolute values are shown, and the charges are normalized to the mass of the particles. See text for detail.

corresponding ion temperature is in the range of 10–15 eV. This again is in a reasonable agreement with the measurements by Collette et al. (2016), where an ion temperature of 23 eV was reported for 20 km/s impacts. For completeness we note that Ratcliff et al. (1997) has reported ion temperatures on the order of 10–50 eV

for a wide range of impact speeds that shows variation with the ion species. The ion energies were calculated from the widths of mass lines measured in a linear time-of-flight analyzer setup. On the other hand, the hydrodynamic simulations of dust impact events performed by Fletcher et al. (2015) predicted significantly lower temperatures (about 4 eV at 20 km/s impact speed) than those reported by Collette et al. (2016), or in this article.

3.4. Effects of the Magnetic Field ($B \neq 0$)

Now let us investigate the variation of the signals with the magnetic field. It is immediately evident from Figure 3 that escaping electrons are strongly influenced by the magnetic field, while escaping ions are not. This fact is a good a posteriori proof that the decomposition of the impact waveforms into electron and ion contributions is appropriate, as one expects only the motion of the electrons being affected by the magnetic field. Further examination reveals that $B_\perp$ has a stronger effect than $B_\parallel$ on suppressing the escape of electrons from the SC. This can be explained as $B_\perp$ is oriented parallel to the plane of the HGA and will retain the free electrons within the dish and thus decreasing their chance for escape. $B_\parallel$, on the other hand, provides the gyrating electrons a path to escape along the field lines toward the dust beam (Figure 1). The effect of $B_\perp$ appears the strongest for 0 V bias and the weakest for −20 V bias. $E \times B$ drift may play a role in the escape of electrons, and of course this drift speed would increase with the bias potential. This effect, however, has not yet been investigated in detail.

Within the gap between Saturn's ionosphere and the D ring, the Cassini spacecraft potential was in the range of +0.5 to −1 V, as indicated by the Langmuir probe instrument onboard. The low and positive potential was possibly the consequence of the presence of negative ions or secondary electron emission from the SC induced by ions or fast neutrals (Morooka et al., 2019; Wahlund et al., 2017). During the closest Saturn approach and the ring plane crossings, the peak value of the magnetic field was 18 μT (Dougherty et al., 2018), which is much larger than the typical ≈10 nT during ring grazing orbits (Arridge et al., 2011). The corresponding electron Larmor radius is $r_L = 0.19$ m, and its ratio to the characteristic size of the SC is $L_{SC}/r_L \cong 20$, where $L_{SC} \cong 4$ m is assumed. The ratios covered in the experiments are similar, $L_{SC}/r_L \cong 20$ and 85 for the 0.35 and 1.45 mT settings, respectively.

The results presented in Figure 3 and the discussions from above allow to make the following conclusions with respect to effect of magnetic field on the dust detection by Cassini's RPWS instrument in the gap between the Saturn's main ring and its atmosphere/ionosphere. The amplitudes of the dust signals are likely significantly reduced. Thus, both the sizes and density of the dust particles deduced from the RPWS data appear deflated by perhaps as much as a factor of 3–5, compared to the +5 V bias case (Figure 3). This reduction appears to be dominantly due to the low SC potential. The ambient magnetic field does reduce the fraction of escaping electrons from the plasma cloud. However, the measured signal is proportional to Q_{col}, that is the difference of the escaping electron and ion charges (equation (4)). Since the escape of ions is less affected by magnetic field, the amplitudes of the antenna signals are not necessarily impacted.

For completeness, it is important to note that the performed experiments have been carried out with iron particles impacting a tungsten surface. Because of the different materials and/or their combinations, some of the characteristics of the expanding impact plasma may be different in the experiments from those encountered in space. These include ion composition, or the characteristic electron and ion temperatures, for example. In addition, the masses of the impacting particles are limited in the experiments by the capabilities of the dust accelerator. Larger particles at high speeds may generate substantial amount of impact plasma, where plasma effects may become more relevant in the antenna signal-generating processes.

4. Summary and Conclusions

Laboratory measurements using a scaled-down SC model and a dust accelerator are now available to simulate relevant physical processes that lead to the generation of dust impact signals on antenna instruments. The motivation for this work was to investigate the effect of a magnetic field on the signals. The presented data analysis has also extended upon previous measurements and introduced a new method for analyzing the data. In this method, with an accompanying simple model, the waveforms are decomposed into contributions from escaping/collected electrons and ions from the dust impact plasma. A good qualitative

understanding of the impact signals is achieved by considering only two fundamental processes, namely, induced charging and charge collection on the SC.

A detailed set of measurements were performed investigating the effect of the bias potential on the SC. The polarity and the magnitude of this potential set the fraction of electrons and ions that are escaping or collected by the SC. The net effect of these processes determines the shape and the amplitude of the shape of the waveforms. The statistical analysis of the data has shown that the amplitude of the collected charge can be significantly reduced, when the bias potential on the SC is small ($\leq$5 V). In such cases, antenna instruments may not provide representative measurements of dust mass and density distributions.

The measurements with magnetic field revealed that the electrons from the impact plasma are significantly affected, namely, that the magnetic field reduces the chance for the electrons to escape and this process also depends on the orientation of the magnetic field and the potential of the SC. On the other hand, the ion signal showed minimal variation with the magnetic field within the range of the investigated field strength. These findings can be explained by the gyromotion of individual particles in the vicinity of the SC, as the ions having much larger Larmor radii. The performed experimental study suggests that for the case of RPWS measurements near the D ring, the low SC potential likely has a stronger effect reducing the electron part of the dust signals than the magnetic field of Saturn.

Acknowledgments
This presented work was primarily supported by NASA's Cassini Data Analysis Program (CDAP), Grant NNX17AF99G. The authors thank Frederick Thayer for the help with setting up the magnetic coils, and David James and John Fontanese for operating the dust accelerator. L. N. and J. P. were supported by the Czech Science Foundation (Project 16-057625). The visit of L. N. at the University of Colorado was supported by the Karel Urbánek Foundation and the Ministry of Education, Youth and Sport of the Czech Republic, under Contract LTAUSA 17066. The authors also thank the International Space Science Institute in Bern, Switzerland, for funding the international team meeting "Physics of Dust Impacts: Detection of Cosmic Dust by Spacecraft and its Influence on the Plasma Environment" and facilitating thus many fruitful discussions. Laboratory data (Nouzák et al., 2019) are publicly available in ResearchGate repository (https://doi.org/10.13140/RG.2.2.18687.36007). The authors thank Paul J. Kellogg and an anonymous referee for their constructive feedback on this article.

References

Arridge, C. S., André, N., McAndrews, H. J., Bunce, E. J., Burger, M. H., Hansen, K. C., et al. (2011). Mapping magnetospheric equatorial regions at Saturn from Cassini prime mission observations. *Space Science Reviews*, *164*(1-4), 1–83. https://doi.org/10.1007/s11214-011-9850-4

Aubier, M. G., Meyer-Vernet, N., & Pedersen, B. M. (1983). Shot noise from grain and particle impacts in Saturn's ring plane. *Geophysical Research Letters*, *10*(1), 5–8. https://doi.org/10.1029/GL010i001p00005

Auer, A., & Sitte, K. (1968). Detection technique for micrometeoroids using impact ionization. *Earth and Planetary Science Letters*, *4*(2), 178–183. http://doi.org/10.1016/0012-821x(68)90013-7

Auer, S. (2001). Instrumentation. In E. Grün (Ed.), *interplanetary dust*, (pp. 385–444). New York: Springer.

Burchell, M. J., Cole, M. J., McDonnell, J. A. M., & Zarnecki, J. C. (1999). Hypervelocity impact studies using the 2 MV Van de Graaff accelerator and two-stage light gas gun of the University of Kent at Canterbury. *Measurement Science and Technology*, *10*, 41–50. https://doi.org/10.1088/0957-0233/10/1/011

Collette, A., Grün, E., Malaspina, D., & Sternovsky, Z. (2014). Micrometeoroid impact charge yield for common spacecraft materials. *Journal of Geophysical Research: Space Physics*, *119*, 6019–6026. https://doi.org/10.1002/2014JA020042

Collette, A., Malaspina, D., & Sternovsky, Z. (2016). Characteristic temperatures of hypervelocity dust impact plasmas. *Journal of Geophysical Research: Space Physics*, *121*, 8182–8187. https://doi.org/10.1002/2015JA022220

Collette, A., Meyer, G., Malaspina, D., & Sternovsky, Z. (2015). Laboratory investigation of antenna signals from dust impacts on spacecraft. *Journal of Geophysical Research: Space Physics*, *120*, 5298–5305. https://doi.org/10.1002/2015JA021198

Dietzel, H., Eichhorn, G., Fechtig, H., Grün, E., Hoffmann, H. J., & Kissel, J. (1973). The HEOS 2 and HELIOS micrometeoroid experiments. *Journal of Physics E: Scientific Instruments*, *6*(3), 209–217. http://doi.org/10.1088/0022-3735/6/3/008

Dietzel, H., Neukum, G., & Rauser, P. (1972). Micrometeoroid simulation studies on metal targets. *Journal of Geophysical Research 77*(8), 1375–1395. https://doi.org/10.1029/JB077i008p01375

Dong, Y., Hill, T. W., & Ye, S.-Y. (2015). Characteristics of ice grains in the Enceladus plume from Cassini observations. *Journal of Geophysical Research:*, *120*, 915–937. https://doi.org/10.1002/2014JA020288

Dougherty, M. K., Cao, H., Khurana, K. K., Hunt, G. J., Provan, G., Kellock, S., et al. (2018). Saturn's magnetic field revealed by the Cassini Grand Finale. *Science*, *362*, eaat 5434. https://doi.org/10.1126/science.aat5434

Fletcher, A., Close, S., & Mathias, D. (2015). Simulating plasma production from hypervelocity impacts. *Physics of Plasmas*, *22*, 093504. https://doi.org/10.1063/1.4930281

Friichtenicht, J. F. (1962). Two-million-volt electrostatic accelerator for hypervelocity research. *Review of Scientific Instruments*, *33*(2), 209–212. https://doi.org/10.1063/1.1746548

Gurnett, D. A., Grün, E., Gallagher, D., Kurth, W. S., & Scarf, F. L. (1983). Micron-sized particles detected near Saturn by the Voyager plasma wave instrument. *Icarus*, *53*(2), 236–254. https://doi.org/10.1016/0019-1035(83)90145-8

Gurnett, D. A., Kurth, W. S., Kirchner, D. L., Hospodarsky, G. B., Averkamp, T. F., Zarka, P., et al. (2004). The Cassini radio and plasma wave investigation. *Space Science Reviews*, *114*(1–4), 395–463. https://doi.org/10.1007/s11214-004-1434-0

Hill, T. W., Thomsen, M. F., Toka, R. L., Coates, A. J., Lewis, G. R., Young, D. T., et al. (2012). Charged nanograins in the Enceladus plume. *Journal of Geophysical Research*, *117*, A05209. https://doi.org/10.1029/2011JA017218

Hsu, H. W., Schmidt, J., Kempf, S., Postberg, F., Moragas-Klostermeyer, G., Seiβ, M., et al. (2018). In situ collection of dust grains falling from Saturn's rings into its atmosphere. *Science*, *362*(6410), eaat3185. https://doi.org/10.1126/science.aat3185

Iglseder, H., & Igenbergs, E. (1987). Measured charge generation by small mass impact at velocities between 1 and 45 km/s. *The International Journal of Impact Engineering*, *5*(1–4), 381–388. https://doi.org/10.1016/0734-743X(87)90055-8

Jacobsen, K. S., Wahlung, J.-E., & Pedersen, A. (2009). Cassini Langmuir probe measurements in the inner magnetosphere of Saturn. *Planetary and Space Science*, *57*(1), 48–52. https://doi.org/10.1016/j.pss.2008.10.012

Kempf, S., Beckmann, U., Klostermeyer, G. M., Postberg, F., Srama, R., Economou, T., et al. (2008). The E ring in the vicinity of Enceladus: I. Spatial distribution and properties of the ring particles. *Icarus*, *193*(2), 420–437. https://doi.org/10.1016/j.icarus.2007.06.027

Kempf, S., Beckmann, U., & Schimdt, J. (2010). How the Enceladus dust plume feeds Saturn's E ring. *Icarus*, *206*(2), 446–457. https://doi.org/10.1016/j.icarus.2009.09.016

Kurth, W. S., Averkamp, T. F., Gurnett, D. A., & Wang, Z. (2006). Cassini RPWS observations of dust in Saturn's E ring. *Planetary and Space Science*, *54*(9–10), 988–998. https://doi.org/10.1016/j.pss.2006.05.011

Meyer-Vernet, N., Moncuquet, M., Issautier, K., & Lecacheux, A. (2014). The importance of monopole antennas for dust observations: Why Wind/WAVES does not detect nanodust. *Geophysical Research Letters*, *41*, 2716–2720. https://doi.org/10.1002/2014GL059988

Meyer-Vernet, N., Moncuquet, M., Issautier, K., & Shippers, P. (2017). Frequency range of dust detection in space with radio and plasma wave receivers: Theory and application to interplanetary nanodust impacts on Cassini. *Journal of Geophysical Research:Space Physics*, *122*, 8–22. https://doi.org/10.1002/2016JA023081

Morooka, M. W., Wahlund, J. E., Hadid, L. Z., Eriksson, A. I., Edberg, N. J. T., Vigren, E., et al. (2019). Saturn's dusty ionosphere. *Journal of Geophysical Research: Space Physics*, *124*, 1679–1697. https://doi.org/10.1029/2018JA026154

Nouzák, L., Hsu, S., Malaspina, D., Thayer, F. M., Ye, S.-Y., Pavlů, J., et al. (2018). Laboratory modeling of dust impact detection by the Cassini spacecraft. *Planetary and Space Science*, *156*, 85–91. https://doi.org/10.1016/j.pss.2017.11.014

Nouzák, L., Sternovsky, Z., Horányi, M., Hsu, S., Pavlů, J., Shen, M.-H., & Ye, S.-Y. (2019). Supplementary data to: "Magnetic field effect on antenna signals induced by dust particle impacts". https://doi.org/10.13140/RG.2.2.18687.36007

Oberc, P. (1996). Electric antenna as a dust detector. *Advances in Space Research*, *17*(12), 105–110. https://doi.org/10.1016/0273-1177(95)00766-8

O'Shea, E., Sternovsky, Z., & Malaspina, D. M. (2017). Interpreting dust impact signals detected by the STEREO spacecraft. *Journal of Geophysical Research: Space Physics*, *122*, 11,864–11,873. https://doi.org/10.1002/2017JA024786

Ratcliff, P. R., Burchell, M. J., Cole, M. J., Murphy, T. W., & Alladfadi, F. (1997). Experimental measurements of hypervelocity impact plasma yield and energetics. *International Journal of Impact Engineering*, *20*(6–10), 663–674. https://doi.org/10.1016/s0734-743x(97)87453-2

Shu, A., Collette, A., Drake, K., Grun, E., Horányi, M., Kempf, S., et al. (2012). 3 MV hypervelocity dust accelerator at the Colorado Center for Lunar Dust and Atmospheric Studies. *Review of Scientific Instruments*, *83*, 075108. https://doi.org/10.1063/1.4732820

Spahn, F., Schmidt, J., Albers, N., Hörning, M., Makuch, M., Seiß, M., et al. (2006). Cassini dust measurement at Enceladus and implications for the origin of the E ring. *Science*, *311*(5766), 1416–1418. https://doi.org/10.1126/science.1121375

Srama, R., & Auer, S. (2008). Low-charge detector for the monitoring of hyper-velocity micron-sized dust particles. *Measurement Science and Technology*, *19*(5), 1–8. https://doi.org/10.1088/0957-0233/19/5/055203

Srama, R., Kempf, S., Klostermeyer, G. M., Helfert, S., Ahrens, T. J., Altobelli, N., et al. (2006). In situ dust measurements in the inner Saturnian system. *Planetary and Space Science*, *54*(9–10), 967–987. https://doi.org/10.1016/j.pss.2006.05.021

Thomas, E., Auer, S., Drake, K., Horányi, M., Munsat, T., & Shu, A. (2013). FPGA cross-correlation filters for real-time dust detection and selection. *Planetary and Space Science*, *89*, 71–76. http://doi.org/10.1016/j.pss.2013.09.004

Vaverka, J., Pavlů, J., Nouzák, L., Šafránková, J., Němeček, Z., Mann, I., & Lindqvist, Per-Arne (2019). One-year analysis of dust impacts like events onto the MMS spacecraft. *Journal of Geophysical Research: Space Physics*, *124*. 8179–8190. https://doi.org/10.1029/2019JA027035

Wang, Z., Gurnett, D. A., Averkamp, T. F., Persoon, A. M., & Kurth, W. S. (2006). Characteristics of dust particles detected near Saturn's ring plane. *Planetary and Space Science*, *54*(9–10), 957–966. https://doi.org/10.1016/j.pss.2006.05.015

Wahlund, J.-E., Morooka, M. W., Hadid, L. Z., Persoon, A. M., Farrell, W. M., Gurnett, D. A., & Vigren, E. (2017). In situ measurements of Saturn's ionosphere show that it is dynamic and interacts with the rings. *Science*, *359*(6371), 66–68. https://doi.org/10.1126/science.aao4134 Ye, S.-Y., Gurnett, D. A., & Kurth, W. S. (2016). In-situ measurements of Saturn's dusty rings based on dust impact signals detected by Cassini RPWS. *Icarus*, *279*, 51–61. https://doi.org/10.1016/j.icarus.2016.05.006

Ye, S.-Y., Gurnett, D. A., Kurth, W. S., Averkamp, T. F., Kempf, S., Hsu, H. W., et al. (2014). Properties of dust particles near Saturn inferred from voltage pulses induced by dust impacts on Cassini spacecraft. *Journal of Geophysical Research: Space Physics*, *119*, 6294–6312. https://doi.org/10.1002/2014JA020024

Ye, S.-Y., Kurth, W. S., Hospodarsky, G. B., Averkamp, T. F., & Gurnett, D. A. (2016). Dust detection in space using the monopole and dipole electric field antennas. *Journal of Geophysical Research: Space Physics*, *121*, 11,964–11,972. https://doi.org/10.1002/2016JA023266

Ye, S.-Y., Kurth, W. S., Hospodarsky, G. B., Persoon, A. M., Sulaiman, A. H., Gurnett, D. A., et al. (2018). Dust observations by the Radio and Plasma Wave Science instrument during Cassini's Grand Finale. *Geophysical Research Letters*, *45*, 101–110. https://doi.org/10.1029/2018GL078059

Ye, S.-Y., Vaverka, J., Nouzák, L., Sternovsky, Z., Zaslavsky, A., Pavlů, J., et al. (2019). Understanding Cassini RPWS antenna signals triggered by dust impacts. *Geophysical Research Letters*, *46*, 10,941–10,950. https://doi.org/10.1029/2019GL084150

Zaslavsky, A. (2015). Floating potential perturbations due to micrometeoroid impacts: Theory and application to S/WAVES data. *Journal of Geophysical Research: Space Physics*, *120*, 855–867. https://doi.org/10.1002/2014JA020635